Pure appl. geophys. 165 (2008) 797–828
0033–4553/08/050797–32
DOI 10.1007/s00024-008-0335-7

Pure and Applied Geophysics

Analysis of the Microseismicity Induced by Fluid Injections at the EGS Site of Soultz-sous-Forêts (Alsace, France): Implications for the Characterization of the Geothermal Reservoir Properties

NICOLAS CUENOT,[1,*] Catherine Dorbath,[2] and LOUIS DORBATH[2]

Abstract—In June/July 2000, a hydraulic stimulation experiment took place at the geothermal EGS site of Soultz-sous-Forêts (Alsace, France) in order to enhance the permeability of the fractured granitic massif at 5 km depth. As it is well known that fluid injections tend to induce microseismic events, a downhole and a surface seismological network have been installed to monitor the seismic activity during the stimulation test. 23400 m^3 of fluid have been injected in the rock volume through the open-hole section (4400 m–5000 m) of the well GPK2 at increasing rates of 30 $l.s^{-1}$, 40 $l.s^{-1}$ and then 50 $l.s^{-1}$. More than 7200 microseismic events in the magnitude range –0.9 to 2.6 have been precisely located through a simultaneous inversion of the seismic velocity structure and location parameters. The analysis of the behavior of the seismicity relative to the hydraulic parameters gives important information about the geothermal reservoir. It appears that the evolution of the seismicity strongly depends on the variations of the injection rate: An increase or a decrease leads to changes of the velocity structure, the number and magnitude of microseismic events. This involves different hydro-mechanical processes between the fluid flow and the fracture planes, which will control the final shape of the microseismic cloud. Moreover, the study of the variations of the *b*-value with time suggests that the stimulation experiment produces a large proportion of small earthquakes, but records of events of magnitude higher than 2 indicate that fluid injection could reactivate structures whose dimensions allow the generation of such earthquakes.

Key words: Geothermal reservoir, hydraulic stimulation, microseismicity, velocity structure, *b*-value.

1. Introduction

In 1987, a European EGS (Enhanced Geothermal Systems) project was founded at the site of Soultz-sous-Forêts (Alsace, France) by France, Germany and the European Commission (KAPPELMEYER *et al.*, 1991). Soultz-sous-Forêts is situated within the central upper Rhine Graben, about 50 km north of Strasbourg (Fig. 1). It is located within the former Pechelbronn oil field, in a zone of large temperature gradient anomaly, which was

[1] Institut de Physique du Globe de Strasbourg (UMR 7516), Ecole et Observatoire des Sciences de la Terre, Université Louis Pasteur, 5, rue René Descartes, 67084 Strasbourg Cedex, France.
E-mail: cuenot@soultz.net

[*] *Present address*: GEIE ''Exploitation Minière de la Chaleur'', Route de Soultz, BP 38, 67250 Kutzenhausen, France.

[2] Institut de Recherche pour le Développement, Ecole et Observatoire des Sciences de la Terre, Strasbourg.
E-mail : catherine.dorbath@eost.u-strasbg.fr

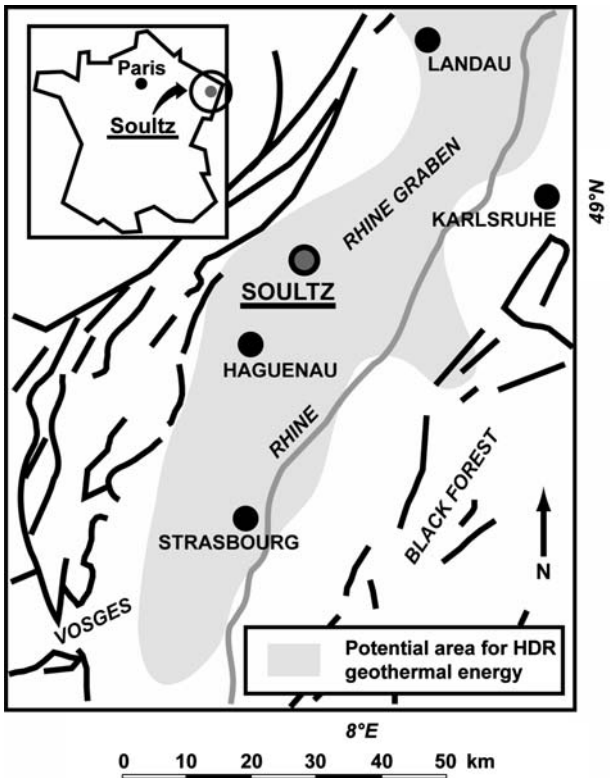

Figure 1
Location of the European Soultz EGS site in the Rhine Graben, Alsace, France (from www.soultz.net).

measured in the subsurface sedimentary layers (SCHELLSCHMIDT and SCHULZ, 1991). These sediment deposits exhibit a thickness of about 1400 m and cover a large granitic rock massif, in which the geothermal reservoir is being developed: The aim is to create an artificial, deep heat exchanger by "stimulating" the natural fracture network. Large-scale water injections can induce shearing on pre-existing joints, which are favorably oriented in the regional tectonic stress field, since the increasing pore fluid pressure is likely to reduce the effective normal stress on the fractures (HEALY *et al.*, 1968; PEARSON, 1981). Most of them are hydrothermally sealed joints (GENTER and TRAINEAU, 1996) but the slipping on fracture plane breaks the sealing and enhances the hydraulic connectivity between the boreholes and the fracture system. This leads to an increase of the permeability, which is one of the main parameters for the optimization of heat transfer between rocks and fluids. For this purpose, two deep boreholes have been drilled into the granitic rocks: GPK1, initially reaching about 2000 m depth, then extended to 3600 m (GARNISH *et al.*, 1994) and GPK2, initially drilled up to 3800 m, then deepened to 5000 m. Since the beginning of the project, several injection and production hydraulic tests have been carried out through

these two boreholes; among them, a large-scale injection test was performed in September 1993 to stimulate GPK1 (e.g., BARIA *et al.*, 1995; JUNG *et al.*, 1995). Induced seismicity has been the subject of numerous studies (e.g., JONES *et al.*, 1995; HELM, 1996; CORNET *et al.*, 1997; PHILLIPS, 2000). In 1995, GPK2 was stimulated for the first time between 3200 m and 3800 m, corresponding to the open-hole section of the well. At this depth, temperature reaches about 170°C. The aim was to improve the connectivity between the two existing wells GPK1 and GPK2, in order to develop a deep heat exchanger. In 1996, GPK2 was stimulated again at similar depth to improve its injectivity with flow rates up to 78 $l.s^{-1}$ (GERARD *et al.*, 1997). Finally in 1997, a following 4-months circulation test revealed a good hydraulic connectivity between both drillholes (GERARD *et al.*, 1997). However, because of temperature requirement for the optimization of the heat exchanger, GPK2 has been deepened in 1999 to a depth of about 5000 m, where rock temperature reaches about 200°C (BAUMGÄRTNER *et al.*, 2000; BARIA *et al.*, 2000). The last large-scale injection test was performed in June/July 2000 through GPK2 after its deepening to enhance the fracture network and the permeability between 4400 m and 5000 m (new open-hole section of the well). WEIDLER *et al.* (2002) reported the main hydrological observations of this experiment, as well as seismological results obtained from the downhole seismic network (see paragraph 2 for a description of the experimental settings).

In this study, we present the results of the microseismicity viewed from the complete seismological network (surface and downhole systems). We will first briefly describe the experimental settings of the 2000 stimulation test (hydraulic parameters, seismological networks and collected data). Then we will focus on the local 3-D tomography (THURBER, 1983) and the spatio-temporal distribution of the seismicity. Since the huge number of recorded events allows us to divide our database into chronological sets, we have been able to highlight clear temporal changes in the seismic velocity structure during the stimulation; furthermore, the precise location of microseismic events obtained from the tomographic analysis helps us to describe the evolution of the seismicity. Finally, correlations between the seismological results (temporal variations of the velocity structure, hypocenters distribution, and temporal evolution of the *b*-value) and hydraulic parameters give us new information with which to characterize the hydromechanical behavior of the geothermal reservoir.

2. The Hydraulic Stimulation of June/July 2000

The well GPK2 is planned to be a producer in the future industrial pilot project. In order to improve the connectivity and permeability of the fractures network between 4400 m and 5000 m, GPK2 was stimulated in June/July 2000 at three rate steps during one week. A total of 23400 m^3 of fluids was injected into the newly drilled open-hole section. Hydraulic parameters such as flow logs and pressure measurements were monitored during the stimulation test (WEIDLER *et al.*, 2002). A following low-rate post-fracturation test was carried out one week later to check the efficiency of the large-scale hydraulic test. Seismic

activity induced by the injections was monitored by both a downhole and a surface network.

2.1. Hydraulic Parameters of the Stimulation Test

Injections started on the 30th of June at around 19h 00 GMT. Fluids were injected at 30 $l.s^{-1}$ during 24 h, 40 $l.s^{-1}$ during 27 h and 50 $l.s^{-1}$ during 90 h (Fig. 2) for a total injected volume of about 23400 m^3 (WEIDLER *et al.*, 2002). 800 m^3 of heavy brine were initially injected into the well to get the highest hydrostatic gradient, followed by a mixture of natural brine and fresh water until the shut-in. One week later, a post-fracturation test was performed at 15 $l.s^{-1}$, 25 $l.s^{-1}$ and 30 $l.s^{-1}$. Unfortunately, technical problems and a worrying rise of the seismic activity lead to a half of this test before its end.

During the main stimulation period, injection started at a rate of 30 $l.s^{-1}$ and induced a quasi-immediate pressure response in the well. The overpressure measured at the wellhead and casing-shoe of GPK2 reached a maximum of 12–13 MPa during the first two steps of the experiment (Fig. 2); it attained a maximum peak, corresponding to the instantaneous response to the increase in injection rate and then slowly decreased. After the rise of the rate to 50 $l.s^{-1}$, the downhole overpressure first reached 13 MPa, but continued increasing to a maximum of 14.5 MPa until the shut-in. During this third phase of stimulation, the behavior of the pressure was then different from the two first steps. Immediately after the end of injection, the pressure dropped instantaneously by about 5 MPa and then began to decline very slowly, suggesting a remaining overpressure in the geothermal reservoir or, at least, in the vicinity of the injection well.

2.2. The Seismological Networks

The microseismicity induced by the injection has been monitored by both a downhole and a surface network. The first one was set up in some observation wells, drilled previously for the seismic monitoring of the 1993 stimulation (CORNET and JONES, 1994; JONES *et al.*, 1995). One additional observation well, OPS4, was drilled in early 2000 to improve the efficiency of the network (JONES, 1999). Thus, five wells were equipped with sensors during the 2000 stimulation (DYER, 2001). Wells 4550, 4601 and OPS4 extended to about 1500 m depth, at the top of the granite. They contained CSMA[1]-type 4-components accelerometer sensors. Two CSMA-type high temperature hydrophones were installed in the wells EPS1 at around 2000 m depth and GPK1 at 3500 m depth. Accelerometers were in tetrahedral configuration with one vertical component and the three others forming an angle of 109.5° between each other. Detection was done by triggering. Sampling rate was 2000 sps/channel and the duration of each recorded signal was 2 s.

[1] Camborne School of Mines Associates, Ltd.

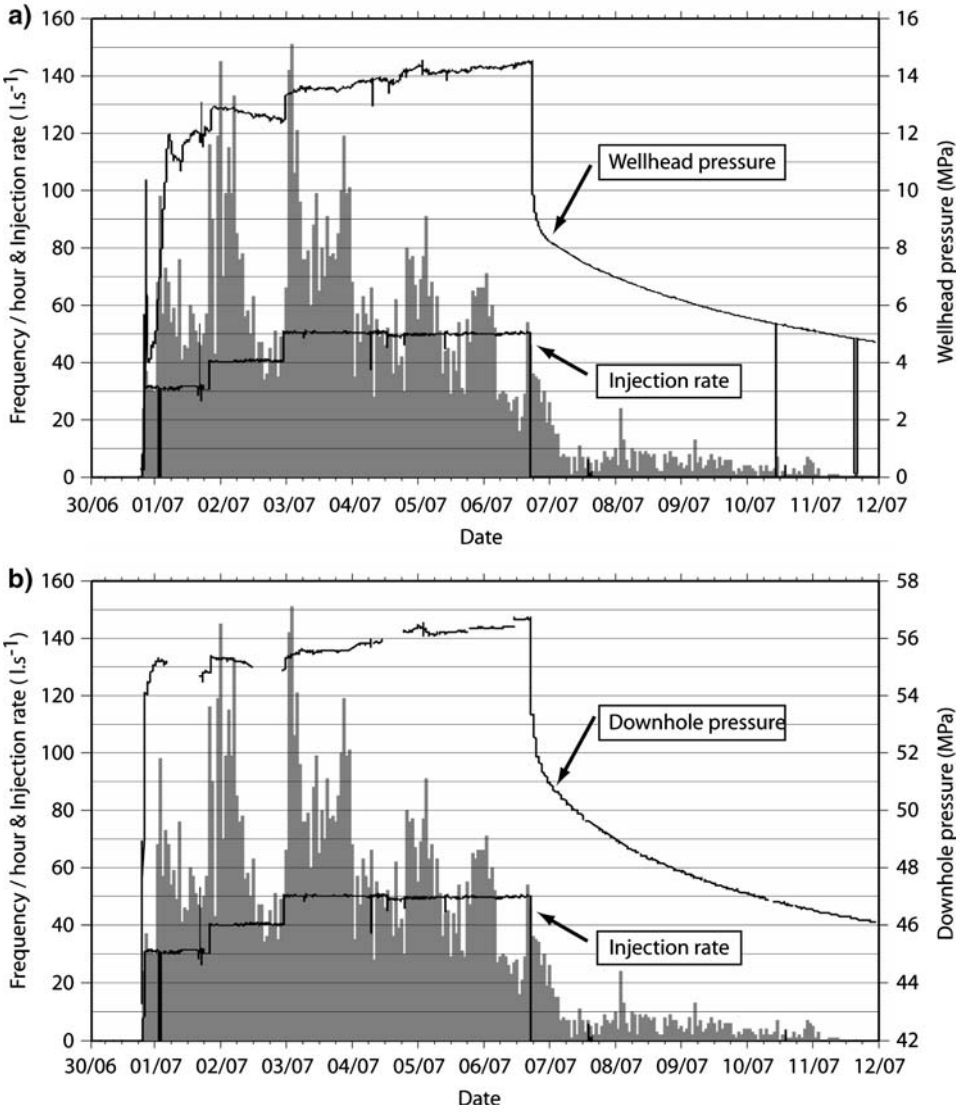

Figure 2
Injection rate and events rate per hour plotted against time during the 2000 stimulation with a) the overpressure measured at the wellhead of the well GPK2 and b) the downhole pressure measured at the casing-shoe of GPK2. Hydrological data from WEIDLER *et al.* (2002).

The surface network was installed by EOST[2], University of Strasbourg, and contained different types of seismological stations. Three of them were permanent stations, belonging to the ReNaSS (French National Seismic Network) and designed to monitor

[2] Ecole et Observatoire des Sciences de la Terre.

Figure 3 ▶

Downhole and surface seismological stations installed during the 2000 stimulation test. a) Plane view of the configuration of both networks. The type of sensor at each station is indicated by different symbol and the wellheads of GPK1 and GPK2 drillholes are plotted on the map. The dashed rectangle shows the zone which is presented in perspective on Figure 3b. b) Three-dimensional view of the borehole geometry and types of downhole sensors. The thick parts of the borehole trajectories correspond to the open-hole sections of the wells. Note that this is a simplified picture: Boreholes trajectories have been drawn vertically, in reality they are deviated at depth. Positions of the downhole hydrophones have been indicated although data from these sensors have not been used in this study.

the local, natural seismicity. One broad-band sensor (Güralp type) was also permanently installed at Soultz-sous-Forêts. In addition, fourteen temporary stations were set up during the stimulation test. Eight were continuously recording, telemetered, 1 Hz, single vertical seismometers. Five were autonomous three-component seismometers recording by triggering. Finally one three-component station was also continuously recording. Acquisition was conducted with a sampling rate of 180 sps/channel. Temporary stations were removed on the 11th of July, i.e., five days after the shut-in. Unfortunately, seismic events still occurred at that time; this was not predictable from previous experiments since no significant seismic activity was observable after shut-in. Therefore, seismicity, which occurred after the 11th of July was only monitored by the permanent stations and the downhole system. In this study, all the calculations have been performed using the complete temporary surface network and the three accelerometers. A map of the stations used in the study is shown in Figure 3. The data from the downhole system were not recorded with the same time reference as the surface network: the simultaneous record of one component of the accelerometer in OPS4 by the permanent surface network during the whole survey solved this problem.

2.3. The Database of Microseismic Events

Among the huge amount of triggered events observed on the downhole network, especially during the injection period, we decided to only keep events, which were clearly recorded by at least five stations from the telemetered surface network, to be sure to actually consider a real event (not a "false" triggering) and to have enough arrival times to perform reliable locations. Thus, each event in our database has been recorded by at least 8 stations (5 from the surface network and the 3 downhole accelerometers). By applying this criterion, we picked manually about 11,000 microseismic events detected on the surface network. For comparison, more than 30,000 triggered events were recorded downhole (DYER, 2001). The difference may be explained by the proximity between downhole stations and seismic sources, some parasitical triggerings on the accelerometers caused by a high underground noise level and the high attenuation of seismic waves reaching the surface due to the 1400 m thick sedimentary layers. The picking errors on surface stations were estimated to be about 0.01 s because of the sampling rate and the clear onset of P and S waves. In Figure 2 is plotted the seismic

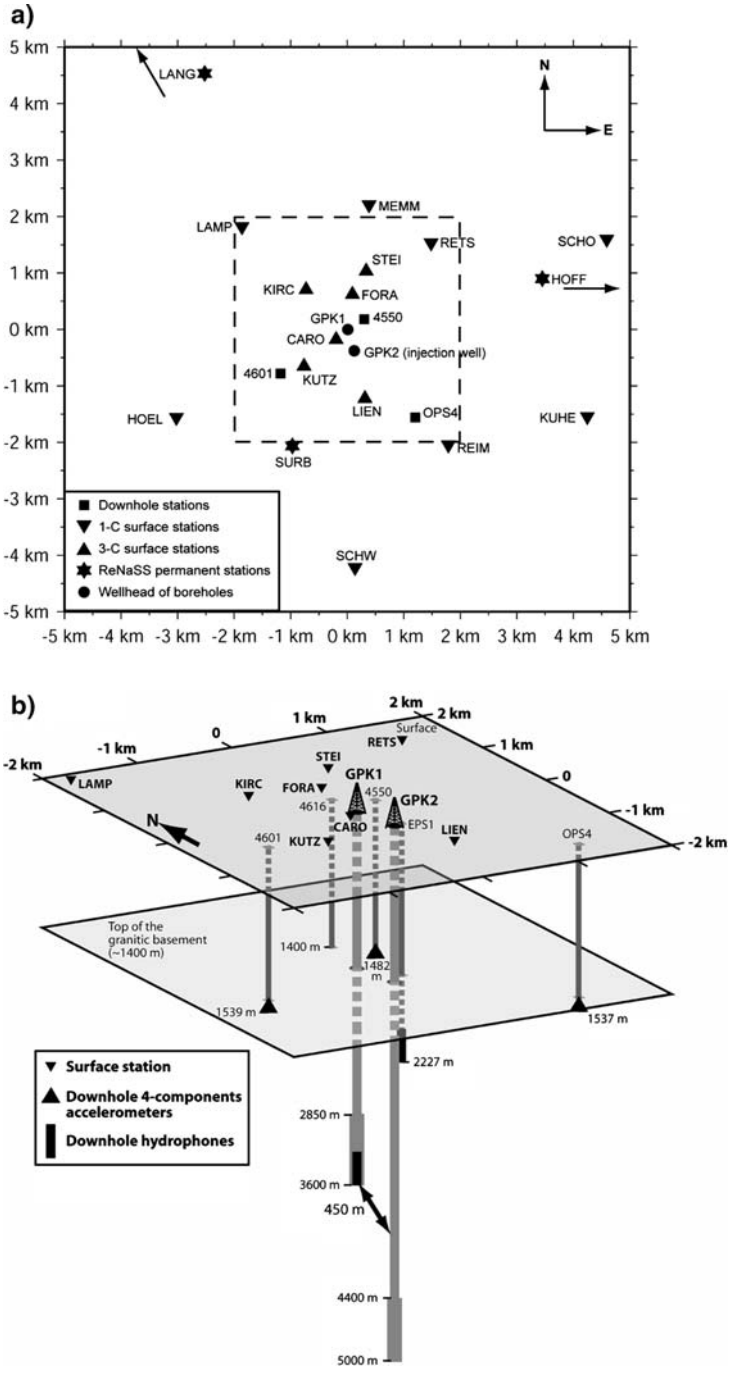
a)
5 km
4 km
3 km
2 km
1 km
0 km
-1 km
-2 km
-3 km
-4 km
-5 km
-5 km -4 km -3 km -2 km -1 km 0 km 1 km 2 km 3 km 4 km 5 km
LANG
N
E
MEMM
LAMP
RETS
SCHO
STEI
HOFF
KIRC
FORA
GPK1
4550
CARO
GPK2 (injection well)
4601
KUTZ
LIEN
OPS4
HOEL
KUHE
SURB
REIM
SCHW
Downhole stations
1-C surface stations
3-C surface stations
ReNaSS permanent stations
Wellhead of boreholes
b)
2 km
1 km
0
-1 km
-2 km
Surface
RETS
STEI
GPK1
LAMP
KIRC
FORA
4550
GPK2
4616
CARO
EPS1
LIEN
OPS4
N
4601
KUTZ
Top of the granitic basement (~1400 m)
1400 m
1482 m
1539 m
1537 m
2227 m
2850 m
3600 m
450 m
4400 m
5000 m
Surface station
Downhole 4-components accelerometers
Downhole hydrophones

event rate together with the injection flow rate and pressure measured at GPK2 wellhead and casing-shoe as a function of time. First, we can observe that there is minimum time delay between the beginning of the injection and the first recorded event. We detected about 30 events during the first hour of the experiment. Then the rate quickly increased to one hundred events per hour and then decreased to a mean of 60 events per hour. Since the rate drop can be observed on the following days, it is probably related to a diurnal modulation of the number of detected events caused by the noise associated with anthropic activity: this lead to a probable, slight under-estimation of the number of the smallest microseisms that occurred during the daytime. Moreover, we can note the remarkable correlation between the increase of flow rate and the sudden increase of the seismic events rate. This suggests an immediate seismic response from the geothermal reservoir to the perturbation caused by the injection. Thus, during the injection period, the seismic activity seems to have the same behavior in response to the increase of flow rate: There is a quasi-instantaneous rise of the number of events (145 events per hour at 40 $l.s^{-1}$, more than 150 at 50 $l.s^{-1}$) followed by a decrease of the activity. Finally, as soon as GPK2 was shut in, the events rate immediately begin to decline. Nevertheless, there is a remaining seismic activity below 10 events per hour until the end of the recording period. This may be correlated with the slow decrease of the pressure, that is, remaining overpressure is still sufficiently large to cause shearing on fractures planes, although it could also be associated with large-scale movements of fluids or aftershock sequence processes. The post-fracturation test (July 13–July 15) also induced an increase of the seismic activity. Despite the early end of this test, a remaining seismic activity was observable with a few events per day during several weeks (DYER, 2001).

Since hypocenters are situated between 4000 m and 5500 m depth and the surface network extends no farther than a few kilometers from the injection point, seismic rays generally reach the surface with a high incidence angle. As a result, we can observe very clear P and S arrivals. High quality signals can be seen on the examples in Figure 4. Therefore once we have combined data from both networks, each event is characterized by at least 8 P-wave arrival times and 3 or 4 S-wave arrival times. Actually, for the great majority of events, more than 12 P-wave arrivals and 5 S-wave arrivals are available.

We performed a preliminary location of the hypocenters to obtain a trial set for the further tomographic inversion. The initial one-dimensional horizontally layered velocity model was derived from sonic logs and calibration shots in the well GPK1 (BEAUCE *et al.*, 1991). So as to get hypocenters locations as precise as possible, we decided to refine the velocity model and to apply station corrections. Both were iteratively calculated by minimizing residual errors at the stations. Among the 11,000 picked events, we decided to keep only those with the most reliable location, i.e., satisfying the following criterion: RMS $\leq$ 0.02 s. Finally, 7,215 well-located events constituted our database. The final mean mathematical location error is about 80 m horizontally and 100 m vertically.

Magnitudes have been determined from the seismic signal duration. They fall in the range –0.9–2.5 for the main recording period (June 30–July 11). However, interestingly,

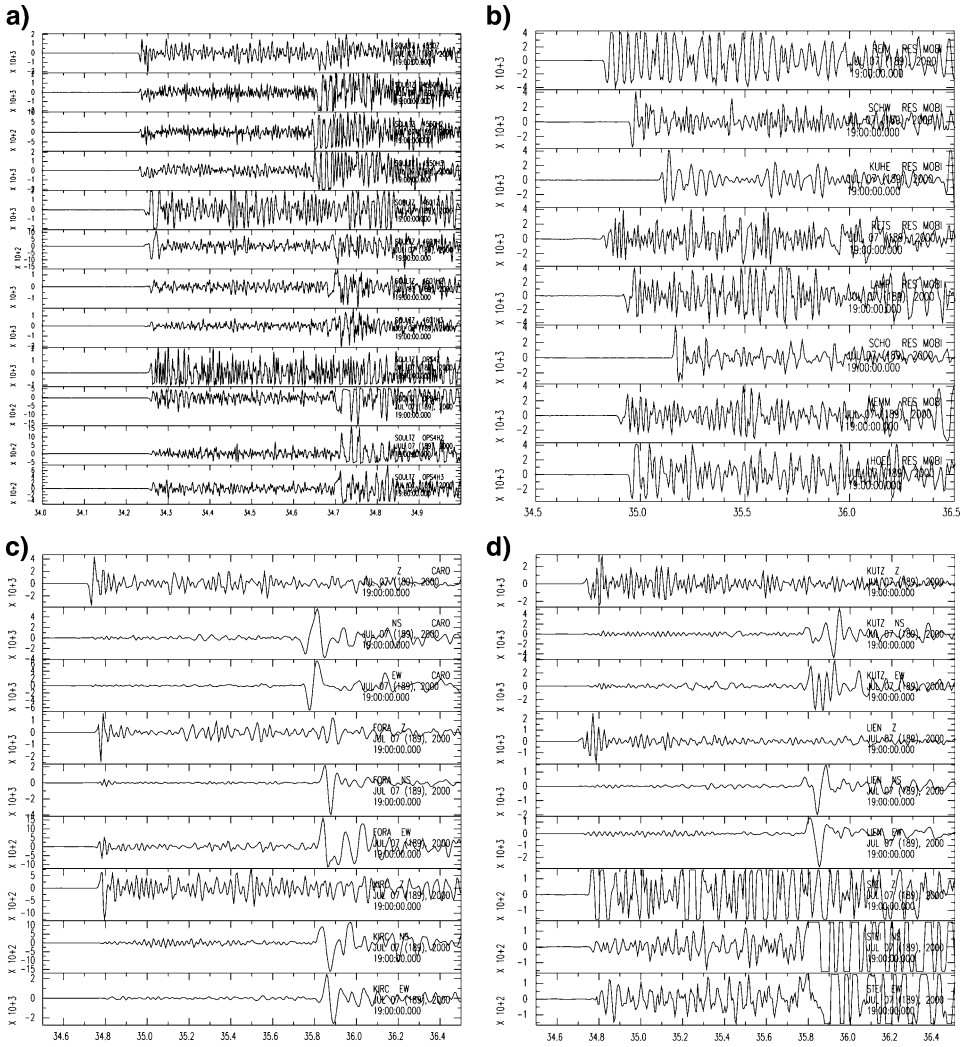

Figure 4
Seismograms of a $M_d = 2.0$ event recorded on the 7th of July, 2000. a) Downhole 4C sensors, b) surface vertical sensors, c) and d) surface 3C sensors. The time window is 2 s long (surface stations) and 1 s long (downhole stations). Note the very clear onsets of P and S wave on each seismogram.

the largest recorded event ($M_d = 2.6$) did not occur during the stimulation, but one day after the end of the post-fracturation test. Events of magnitude smaller than –0.9 probably occurred, however the detection level of the sensors and the strong attenuation due to the sedimentary cover did not allow us to record lower level of magnitude. Figure 5 presents the frequency-magnitude distribution (GUTENBERG and RICHTER, 1944) of the events during the stimulation period. The deviation of the slope from linearity for the lowest

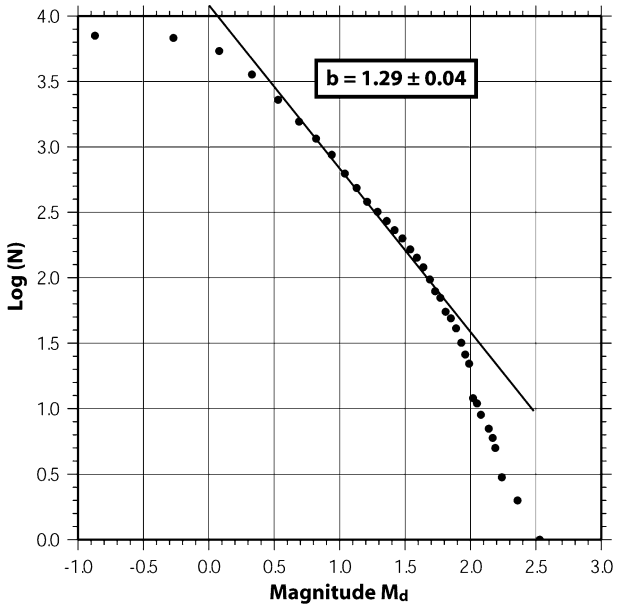

Figure 5
Frequency-magnitude distribution of the events during the whole stimulation period. Maximum likelihood estimate of the *b*-value is indicated.

magnitudes indicates a minimum magnitude of completeness of 0.4. We used the maximum likelihood estimate of AKI (1965) to calculate the *b*-value given by:

$$-b = \frac{\log_{10} e}{\bar{M} - M_{\min}}, \tag{1}$$

where $\bar{M}$ is the average magnitude and $M_{\min}$ the minimum magnitude in a given sample. 7,062 events were included to determine the *b*-value; it is less than the total number of earthquakes in the database, since we were not able to determine the duration magnitude of microseisms in several cases, especially when two events occurred in a time interval of a few seconds. We found a *b*-value of 1.29 ± 0.04 for the entire recording period. It exhibits a rather high value, which is commonly observed in a volcanic area near active magma chambers (e.g., WYSS *et al.*, 2001; MURRU *et al.*, 1999) or in a geothermal area, since the increase of *b*-value is often associated with the presence of fluids in the fractures zone and thus high pore pressures. As a comparison, HELM (1996) calculated the *b*-value for the seismicity induced by the 1993 stimulation experiment at Soultz-sous-Forêts and recorded by a surface network. His study yielded a *b*-value of 1.26, which is consistent with our estimate. Thus in the case of the stimulation experiment, the injection leads to a large production of small magnitude events, with a strong deficit in larger magnitude events, especially above $M_d = 1.8$. Variations of the *b*-value during the stimulation, due to a change in the injection rate, will be discussed later.

3. Velocity Structure and Evolution of the Microseismicity from Local Tomographic Inversion

Fluid injection experiments, as well as volcanic swarms, lead to a high concentration of induced hypocenters within a restricted seismogenic volume. Thus, the identification and interpretation of the evolution of the seismicity and associated structures strongly depend upon the accuracy of location. Several methods have been proposed to highlight seismogenic structures within a dense cloud of microseismic events. Among them, statistical approaches like the "collapsing" method (JONES and STEWART, 1997), provide images of possible structures with the assumption that they are simple. The Joint Hypocentral Determination (JHD) inversion has successfully contributed to an improvement of the imaging of seismogenic structures through improved velocity modelling (e.g., PUJOL, 1992). FEHLER *et al.* (2000), incorporated the collapsing method as a constraint into their JHD inversion and obtained enhanced locations of events which occurred at the Fenton Hill Hot Dry Rock geothermal site. Relative relocation based on waveform cross-correlation techniques (e.g., GAUCHER *et al.*, 1998; MORIYA *et al.*, 2002) is also a powerful tool to increase the accuracy of hypocenter location. ROWE *et al.* (2002) demonstrated otherwise that reducing the picking inconsistencies before using a well-defined velocity model and a sophisticated location method could greatly enhance the reservoir imaging.

In addition to the need of a very precise hypocentral location, we wanted to investigate the influence of the fluid injection on the seismic velocity structure. Thus, we decided to perform a three-dimensional local tomography applying the method of THURBER (1983), which allows a simultaneous inversion to retrieve both the seismic velocity parameters and the hypocentral parameters in a 3-D laterally heterogeneous medium: The determination of locations takes into account the evolution of the velocity structure at each iteration. In the case of the stimulation test, the choice of a tomographic method allowing temporal variations of the seismic velocity is justified by the fact that the injection of several thousands cubic meters of fluids into the reservoir within a relatively short period should have perturbed the rocks physical properties and especially the seismic velocities. Furthermore, since we built a database containing more than 7,200 events, well distributed over the complete recording period, we can actually obtain a temporal evolution of the velocity model which will be compared to the main hydraulic parameters.

3.1. Method

We decided to apply the algorithm SIMULPS12 (EBERHART-PHILLIPS, 1993; EVANS *et al.*, 1994) based on the method of THURBER (1983), for the reasons described previously and because it is especially adapted to a local seismic network geometry and local earthquakes taking place within the studied volume.

The method is based on the resolution of the linearized equation (2) linking the arrival time residuals to the velocity and hypocentral parameters changes for an earthquake at a given station. There are as many equations as the number of arrival times:

$$r = \Delta t_i + \frac{\partial t}{\partial x_i}\Delta x_i + \frac{\partial t}{\partial y_i}\Delta y_i + \frac{\partial t}{\partial z_i}\Delta z_i + \sum_{n=1}^{N}\frac{\partial t}{\partial v_n}\Delta v_n \tag{2}$$

where r is the arrival time residual; Δt_i, Δx_i, Δy_i and Δz_i are the perturbations to the origin time and location parameters, Δv_n is the perturbation to the seismic velocity structure parameters. $\partial t/\partial x_i$, $\partial t/\partial y_i$, $\partial t/\partial z_i$ and $\partial t/\partial v_n$ are the partial derivatives of the arrival time with respect to the event coordinates and velocity parameters. N is the total number of velocity parameters that are defined at the nodes of a three-dimensional mesh. For each event recorded at L stations, equation (2) is written in matrix notation as:

$$r_i = H_i \cdot \Delta h_i + M_i \cdot \Delta m \tag{3}$$

r_i is the vector containing the L residuals, Δh_i is a vector containing the four hypocentral parameter perturbations for the ith event and Δm is the vector of N velocity parameters adjustments. H_i and M_i are the matrices of the partial derivatives.
The resolution of this system is achieved by introducing a matrix Q_0 such as:

$$Q_{0^T} \cdot H_i = 0 \tag{4}$$

So Q_0^T operating on equation (3) yields:

$$r_i^{'} = M_i^{'} \cdot \Delta m. \tag{5}$$

This new set of equations is solved using damped least-squares and the velocity parameter perturbations are introduced into the model to relocate iteratively and individually the earthquakes. Finally, velocity at a given point is calculated by interpolating the velocities at the surrounding grid points.

In order to observe the temporal evolution of the velocity structure, we divided our database into chronological sets of 500 events. We decided to apply the tomographic method to equally populated sets rather than cutting our database into samples of equal duration, because some recording periods exhibit a lesser rate of seismic activity, especially after the shut- in. Thus, for those periods, the rays' coverage would have been insufficient to perform a reliable tomography.

Table 1 shows the fourteen samples of events used in the study, with their corresponding duration and the number of P- and S-wave arrivals involved in the calculation for each set. The last sample contains about 700 events instead of the 500 constituting each other set. Because of the strong decrease of the seismic activity after the shut-in, we preferred to build a larger sample including the five last days of records rather than having an additional set with only 200 events for the reason described in the above paragraph. We used the initial locations of events as trial coordinates for the computation.

Table 1

Events samples with their corresponding duration and number of available P and S-wave arrivals

Sample number	Duration	Number of arrival times	
		P wave	S wave
1	30/06/00 @ 19 h15 - 01/07/00 @ 08 h16	5739	2263
2	01/07/00 @ 08 h17 - 01/07/00 @ 19 h46	5840	2140
3	01/07/00 @ 19 h46 - 02/07/00 @ 03 h18	5198	2305
4	02/07/00 @ 03 h21 - 02/07/00 @ 12 h12	5098	2488
5	02/07/00 @ 12 h17 - 03/07/00 @ 04 h26	5044	1707
6	03/07/00 @ 04 h36 - 03/07/00 @ 13 h58	5428	1875
7	03/07/00 @ 13 h59 - 03/07/00 @ 20 h22	5933	2523
8	03/07/00 @ 20 h23 - 04/07/00 @ 04 h23	5606	2373
9	04/07/00 @ 04 h26 - 04/07/00 @ 17 h09	4940	2111
10	04/07/00 @ 17 h18 - 05/07/00 @ 02 h55	5076	1965
11	05/07/00 @ 03 h00 - 05/07/00 @ 15 h41	5568	2290
12	05/07/00 @ 15 h43 - 06/07/00 @ 01 h04	6336	2757
13	06/07/00 @ 01 h07 - 06/07/00 @ 16 h30	6038	2955
14	06/07/00 @ 16 h32 - 11/07/00 @ 05 h58	6422	2989

Moreover, the calculation process also requires a trial velocity model: The one-dimensional input model is the one we used and refined during the first location step. Table 2 shows the P- and S-wave initial seismic velocities as a function of depth. We did not include any lateral velocity variation in the input model. The studied rock volume is gridded with an irregular mesh of 2.2 km $\times$ 3 km $\times$ 7.6 km in the x (eastward), y (northward) and z (depth) directions. Figure 6 presents a plane view of the mesh superimposed on the final microseismic cloud. The numbered nodes refer to the points where velocity variations are plotted versus time on Figure 8 (see following paragraph). Horizontal nodes spacing is 200 m in the x and y directions near the center of the grid, where most of the hypocenters lie and where a maximal resolution is required. Near the borders of the mesh, grid points are only spaced by 400 m, because the microseismic cloud is concentrated in the middle of the grid. In the vertical direction, we

Table 2

Input 1-D layered velocity model used as a trial model in the tomographic calculations

Depth (km)	V_P (km.s^{-1})	V_S (km.s^{-1})
0.0	1.85	0.86
0.8	2.87	1.34
1.6	5.80	3.31
2.6	5.82	3.32
3.6	5.85	3.34
4.6	5.87	3.35
5.6	5.90	3.37
6.6	5.92	3.38
7.6	5.95	3.40

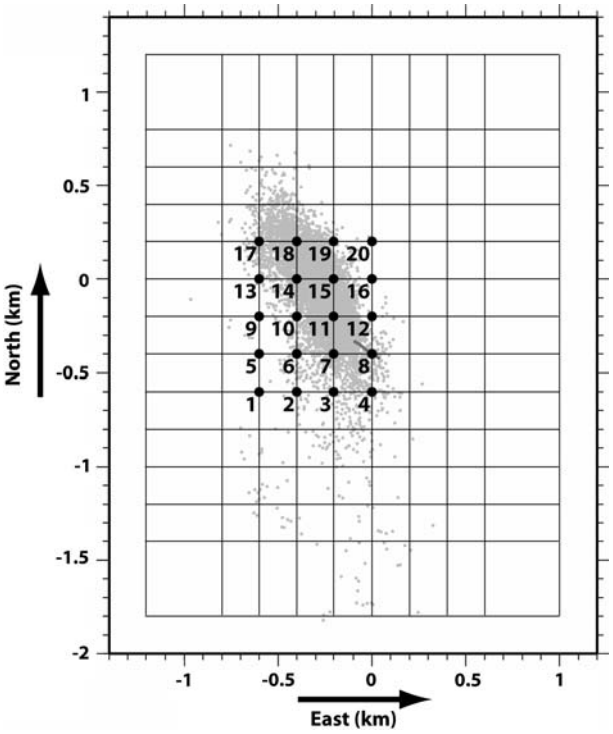

Figure 6
Plane view of the mesh used for the tomographic inversion. Horizontal extension of the grid is 2.2 km × 3 km in the X (east) and Y (north) directions, respectively. The microseismic cloud is plotted to outline zones where a good resolution is needed. Thus nodes are spaced by 200 m at the center of the mesh and 400 m near the outer boundaries of the studied zone. The numbered black dots show the nodes where we plot the temporal evolution of the velocity on Figure 8.

positioned the first grid points at 0.0 km, 0.8 km and 1.6 km. This range corresponds to the main sedimentary layers. At a depth of 1.6 km, the top of the granite massif is reached. Since we assume that there are considerable less velocity variations with depth in the granite than in the horizontal directions, the vertical spacing is fixed to 1 km. In the following, we will only discuss the results for the P-wave velocity: as seen in Table 1, the number of S-wave arrival times is insufficient to obtain a good resolution. The P-wave data variance is reduced by 75% to 85%, depending on the set. As regards the location errors, the average RMS after calculation is 0.01 s. We assume a mean location error less than 50 m horizontally and about 80 m vertically.

3.2. Temporal Evolution of the V_P Velocity Structure

A sequence of fourteen successive images was computed to observe the evolution of the V_P velocity in the geothermal reservoir (Fig. 7). The corresponding 500 events used

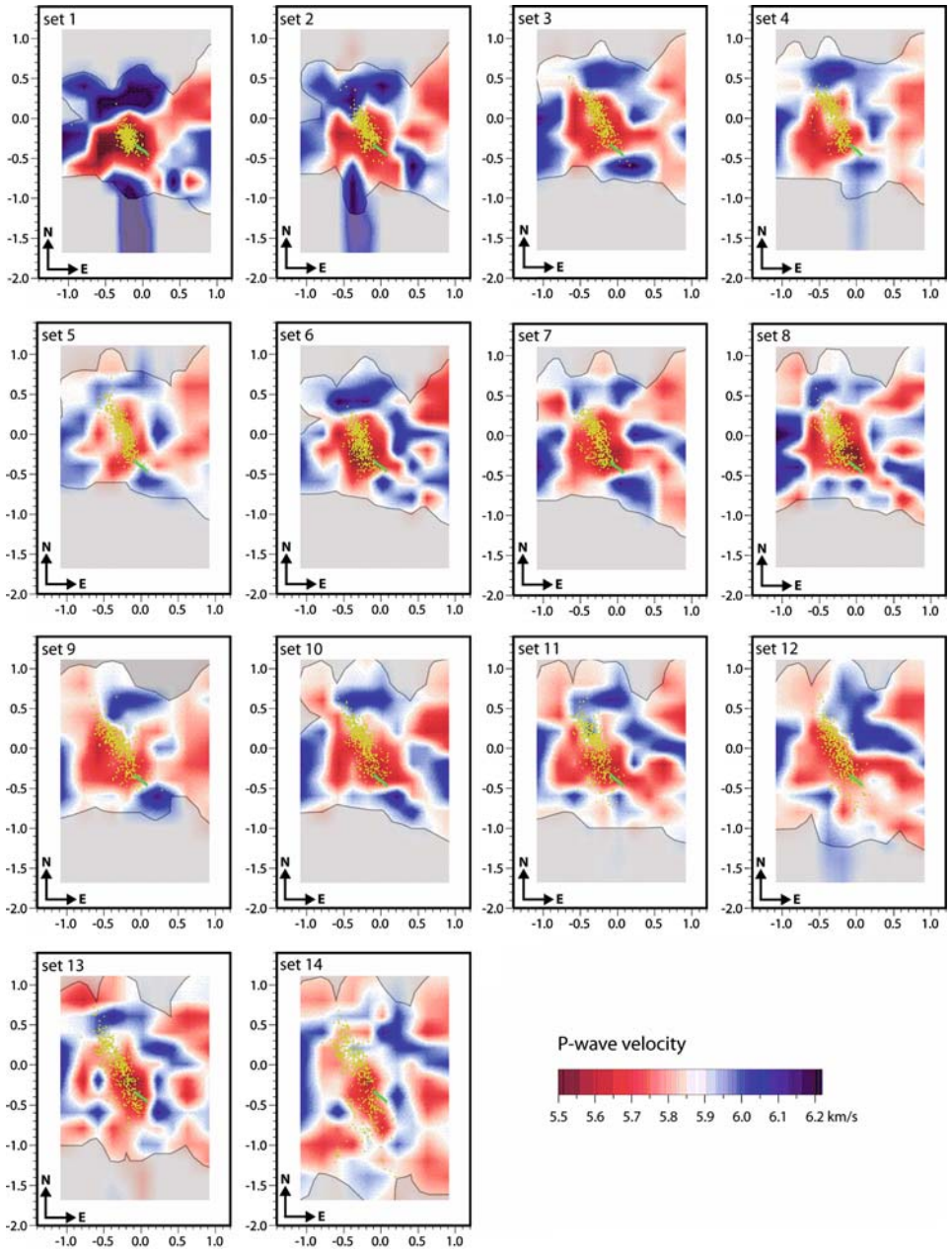

Figure 7

Evolution of the P-wave seismic velocity at 4.6 km depth during the 2000 stimulation test. Images are in chronological order from set 1 to set 14. Yellow dots represent the 500 events used in the computation for each subfigure. The green line corresponds to the open-hole section of the injection well GPK2. Grey areas need not be considered as they define zones of poor resolution.

for the calculation are plotted on each map to outline the shape and position of the microseismic cloud at that time. The trajectory of the open-hole section of the well GPK2 is also indicated: it has been measured through a gyroscopic survey performed by the Scientific Drilling company for Socomine[3]. The measured depth error on the well trajectory was 3 m and the horizontal uncertainties were about 4 m in the N-S direction and 3 m in the W-E direction. Grey zones do not have to be considered as they correspond to low-resolution areas. Since hypocenters are situated within the studied volume, we have a direct access to the absolute seismic velocities in the medium through the tomography, instead of relative variations from reference velocities. However, the induced seismic activity began just after the beginning of the injection and the region is seismically rather quiet: Therefore, we were unfortunately not able to perform a tomography before the stimulation test. It could have given essential information about the steady state in the reservoir and could have been a reference for comparison with the variations of the velocity structure during the experiment. Nevertheless we can specify some initial conditions before stimulation. The granitic massif exhibits a low, natural permeability, which allows natural fluid flow through the rock mass, mainly through large fracture zones. This was confirmed by the observation of highly hydrothermally altered zones in the granite (e.g., TRAINEAU *et al.*, 1991; GENTER *et al.*, 1997) and a natural, artesian productivity of the wells, whatever depth they reach (JUNG, 1991; BARIA *et al.*, 1995; 2001). Thus before the test, the rocks are not dry but contain hot brine. Moreover the only disturbances undergone by the rock volume at the depth of the stimulation (4400 m – 5000 m) have been mainly caused by the deepening of GPK2 to 5000 m depth and also by several small-scale hydraulic tests in August 1999, October-December 2000 and February 2000. Temperature logs performed before and after the drilling period demonstrated that the drilling operations did perturb the thermal equilibrium of the surrounding rocks (PRIBNOW *et al.*, 1999). However additional temperature tests, which were carried out in February 2000, that is, four months before the simulation, showed that the granite almost recovered its thermal equilibrium at that time (BARIA *et al.*, 2001).

Figure 7 presents the temporal evolution of the velocity structure at a depth of 4.6 km, corresponding to the location of the stimulated rock volume. Set 1 is calculated using the 500 first events of the stimulation. The dark red color clearly denotes a significant low-velocity anomaly: The plotted microseismic cloud indicates that this anomaly corresponds to the geothermal reservoir. It is difficult to interpret this first result, as we cannot compare the present situation to that before the beginning of the injection: is the anomaly directly due to the start of the stimulation or does it really exist before? Set 2 to set 5 show a slight increase of the velocity from 5.6 $km.s^{-1}$ to about 5.8 $km.s^{-1}$. This observation also appears on Figure 8, which presents the evolution of the V_P seismic velocity at each node of the grid: the group of nodes which are located in the closest area of the injection well (nodes 7, 8, 10, 11, 12 especially) shows a similar evolution of

[3] Socomine was, at that time, the name of the operating company at the geothermal site of Soultz-sous-Forêts. It is now called European Economic Interest Group (EEIG) "Heat Mining".

velocity for the five first sets. This could be related to the conjugate effect of the progressive cooling of the medium due to the introduction of a great quantity of cold fresh water and of the gradual to full fluid saturation of the rock mass. This last parameter is rather important: NUR and SIMMONS (1969) reported from laboratory measurements an increase of the P velocity up to 40% for a fully saturated volume in various granite samples. The saturation-dependent velocities property has been observed by several authors in granite and various types of porous rocks with different types of saturating fluids (e.g., KING, 1966; TODD and SIMMONS, 1972; WYLLIE *et al.*, 1956, 1958). It could also explain the common feature that appears on nodes 13, 16, 17, 18, 19 and 20 (Fig. 8): one can observe a large decrease of the velocity for the three first sets. These nodes are farther from the injection well, indicating that this region may not be subjected to fluid saturation at the beginning of the test. An interesting feature appears between set 5 and set 6: In the picture 7 one can notice the reappearance of the dark red color at the place of the geothermal reservoir, indicating a sudden decrease of the P velocity of about 0.2 $km.s^{-1}$. It is also clear on Figure 8: Nodes 6 to 16 exhibit the decrease of velocity (with more or less amplitude) between set 5 and set 6. However the northernmost area does not seem to be greatly affected. Then, until the end of the recording period, velocity slowly increases in the same way as the beginning of the experiment. This is true for most observation points, except nodes 3 and 4: As described in the following paragraph, microseismic activity appears only lately in this southern zone in the course of the test, implying different or delayed processes. What does induce the quick decrease of the velocity? It appears from the injection curve (Fig. 2) that set 6 contains events which occurred just after the increase of the injection rate to 50 $l.s^{-1}$. We did not indeed observe such a variation between set 3 and set 4, although the injection rate was incremented from 30 $l.s^{-1}$ to 40 $l.s^{-1}$ between these periods. Nevertheless, we found clear correlations between the increase of injection rate up to 50 $l.s^{-1}$ and the change in the hydrological parameters and seismic activity evolution that we cannot observe after the augmentation from 30 $l.s^{-1}$ to 40 $l.s^{-1}$. This would mean that, in order to explain the decrease of the P-wave velocity, we must take into account other parameters which act oppositely from cooling and fluid saturation and which effects on the material are greatly related to the injection rate. WYLLIE *et al.* (1958), CHRISTENSEN and WANG (1985), and NUR (1987) studied the effect of pore pressure on the seismic velocities in dry and saturated rock samples. They found that increasing the pore pressure tends to reduce the P- and S-wave velocity in both cases, as it counteracts the confining pressure. In our experiment, the increase of injection rate to 50 $l.s^{-1}$ induced an overpressure of more than 1 MPa to 2 MPa (Fig. 2). If the observed overpressure is due to a pore pressure increase, then it could explain the observed lowering of P velocity.

Another parameter is likely to induce changes of velocity. As the medium is highly fractured with a dominant orientation, anisotropy should be considered and may vary because of the injections. DELÉPINE (2003) studied the shear-wave splitting on a signal recorded both on downhole and surface stations. The difference between the fast and the slow S wave varies between 0 and 0.04 s for the complete set of records. This does not

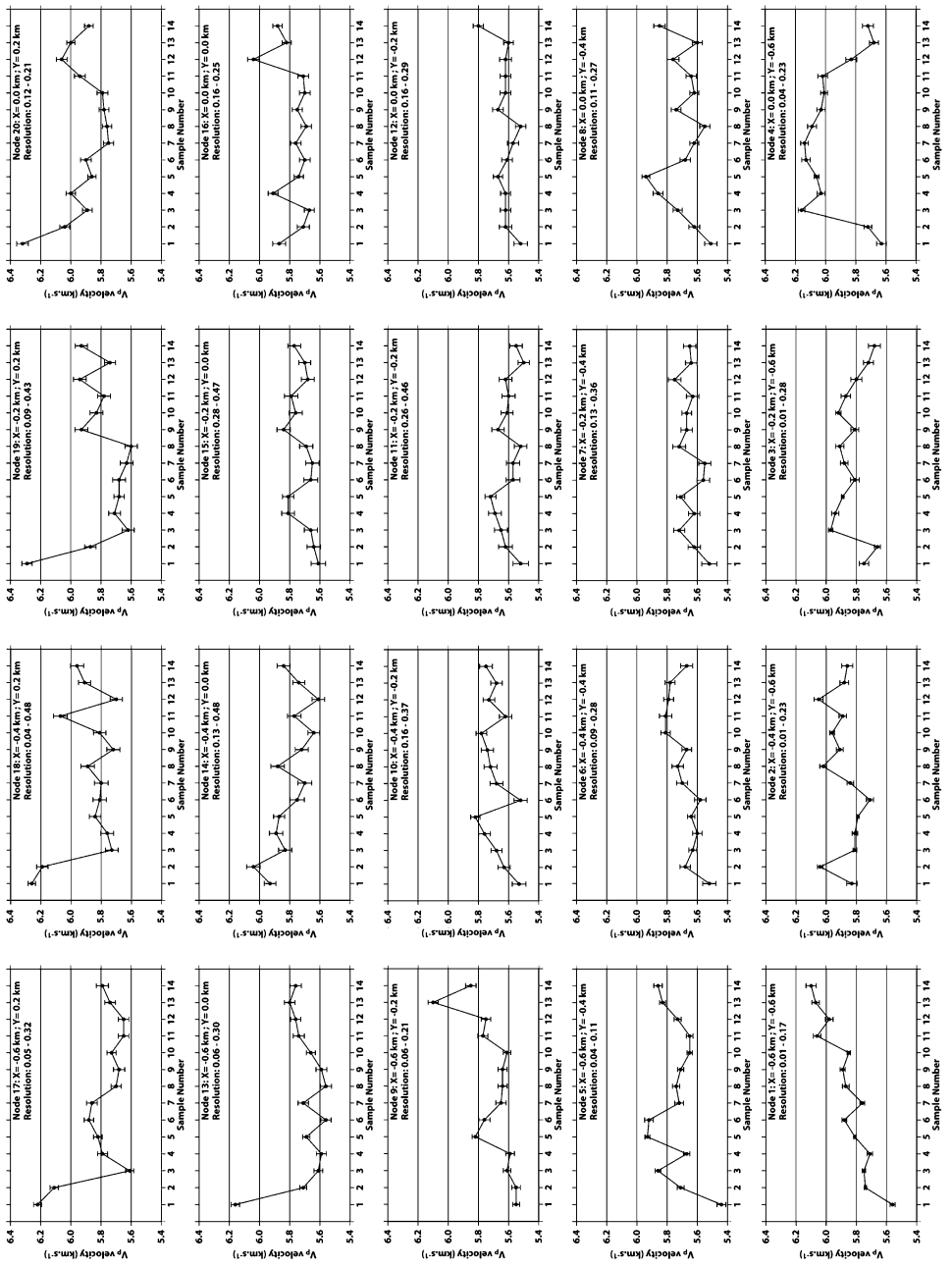

imply a great effect of anisotropy. Furthermore, DELÉPINE (2003) does not observe significant changes of the S-wave splitting during the course of the stimulation test: Anisotropy parameters appear not to be greatly influenced by the injections. Thus, in

◀ Figure 8
Temporal evolution of the P velocity at different points of the grid. The position of the nodes, for which the variations of velocity are plotted here, is indicated on Figure 6. The spatial organization of the above pictures follows the disposition of the points defined on Figure 6 (that is, for example: The picture for the node 1 is on the lower-left corner of the figure, as node 1 is on the lower-left corner of the scheme on Figure 6). For each picture the position of the node is nevertheless reminded (with coordinate X: East direction and coordinate Y: North direction). On each graph, the lowest and highest values of resolution for the 14 estimates of velocity is indicated. Values of velocity are plotted together with their error bars.

order to explain the behavior of the reservoir, we mainly have to focus on the other previously described parameters.

Indeed, correlations between changes in the behavior of these different parameters and the influence of injection rate will be analyzed in the discussion.

3.3. Evolution of the Microseismic Cloud during the Stimulation Experiment

The simultaneous inversion allows us to obtain precise locations of events as the temporal evolution of the seismic velocity structure is taken into account in the computation of the hypocentral parameters. Final results of the location are shown in Figures 9 (a,b,c). On the three pictures, the radius of each circle is proportional to the magnitude of the corresponding event. The trajectory of the open-hole section of the well GPK2 is also plotted as a black line. Figure 9a shows a horizontal plane view of the microseismic cloud. It exhibits an overall elliptic shape, whose maximal extension axis is 1.5 km–2 km long and orthogonal axis is about 0.5 km. It trends in a N30°−35°W direction. A very dense seismicity forms the main part of the cloud and several events that are more isolated appear to the south. Pictures 9b and 9c are vertical cross sections of the cloud viewed in the azimuth N55°E (minimum extension direction) and N145°E (maximal extension direction). They reveal that the 3-D shape of the cloud is a rather flat ellipsoid. It extends between 4 km depth to 5.5 km depth. One can note the very sharp top and bottom boundaries of the cloud: No upward and downward migration of the hypocenters above 4 km depth and below 5.5 km depth has been observed. It suggests the presence of structures avoiding the seismicity to migrate. In the case of the stimulation experiment, it means that, either these structures could be impermeable to the pore pressure transfers and/or fluid circulation or, on the contrary, a highly permeable zone could be present, which allows easy fluid flow, implying no significant overpressure increase and thus no microseismic activity.

This observation reveals the need to study the evolution of the seismicity during the injections, since areas of seismic activity development correspond to high fluid pressure zones, as shown by Cornet and Yin (1995): this aids better understanding of the phenomenon of fluid pressure migration in the geothermal reservoir. This is a fundamental point, because the reservoir creation and thus the success of the stimulation depend on the enhancement of the fracture network permeability and connectivity, which is accomplished by forcing the fractures to shear by increasing the pore pressure. Figure 10

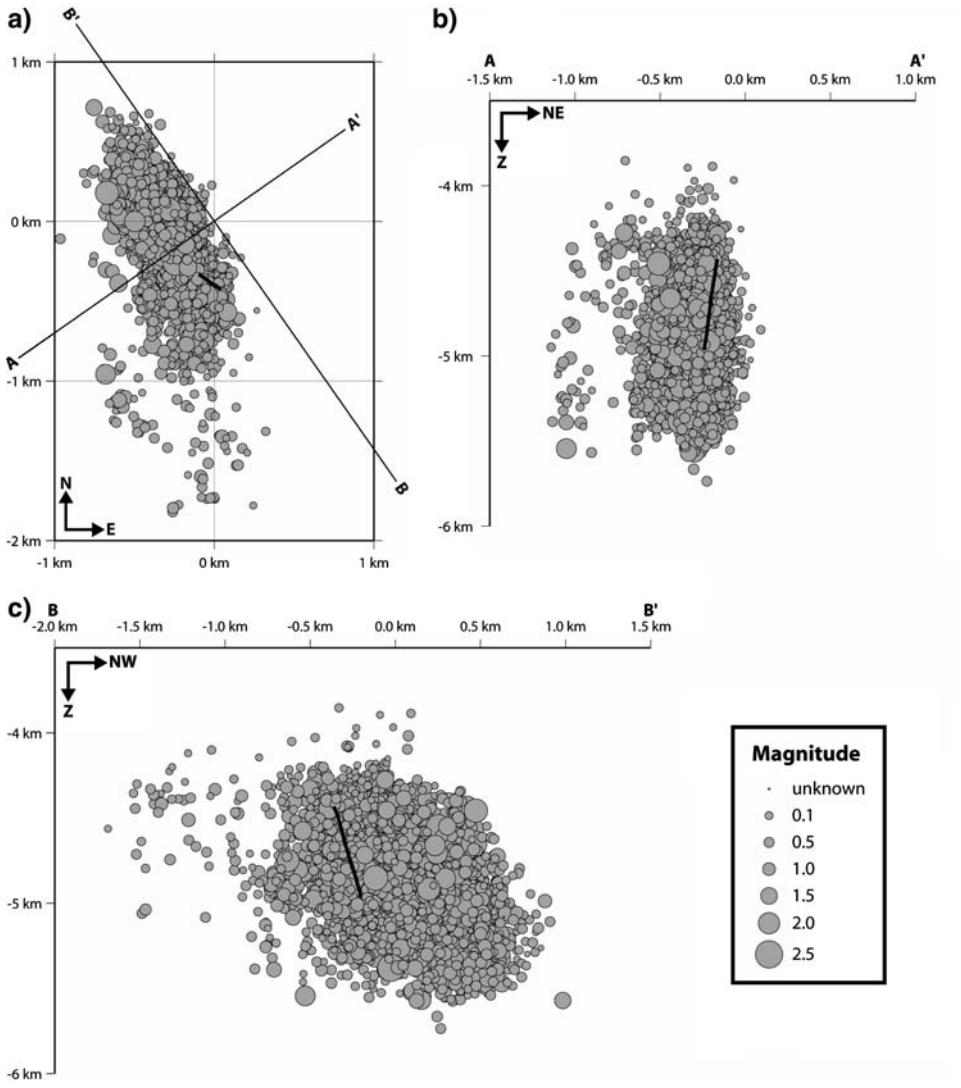

Figure 9

Final location of the whole database of microseismic events. The radius of each circle is proportional to the magnitude. On each plot, the thick black line corresponds to the open-hole section of the injection well. a) Horizontal projection of the microseismic cloud; Profiles AA' and BB' corresponds to the cross sections b) and c). b) Projection of the microseismic cloud on profile AA' of azimuth N55°E (minimum extension of the cloud). c) Projection of the microseismic cloud on profile BB' of azimuth N145°E (maximum extension of the cloud).

presents the temporal evolution of the microseismic cloud. Each picture represents the 500 event locations calculated through the simultaneous tomographic inversion. The radius of the circles is still proportional to their magnitude, and the trajectory of the open-hole

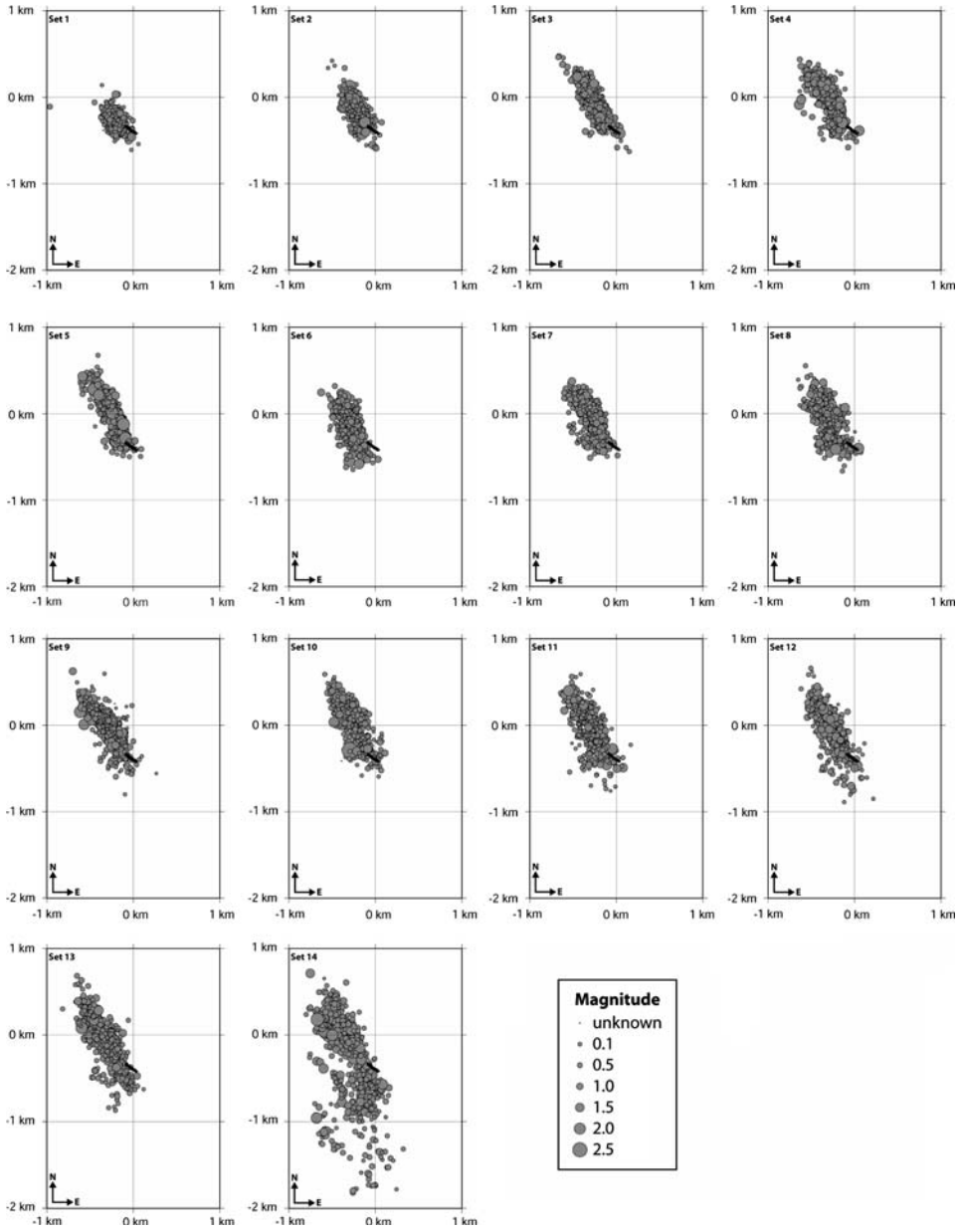

Figure 10

Evolution of the microseismic cloud. Each picture shows each set of 500 events (700 events for the last picture) used in the computation of the local tomography in chronological order. The radius of each circle is proportional to the magnitude and the open-hole section of the injection well is indicated as a thick black line.

section of GPK2 is shown as a black line. The 500 first events of the stimulation test are plotted on picture 10.1. They are concentrated near the injection well but tend to develop to the north-west. Between set 1 and set 5 the microseismic cloud grows up to the north-west however we can only observe a few seismic events occurring to the south of the injection well. At that time, the cloud is elongated in a NW-SE direction and quite thin. Between set 6 and set 11 the behavior of the seismic activity changes: No occurrence of an event farther to the north-west can be noticed, as if the migration of hypocenters in this direction was more or less suddenly stopped. Nevertheless, numerous microseismic events still occur at the place of the geothermal reservoir in already stimulated zones, which form a more concentrated cloud. Some scattered events already begin to appear to the south. The strongest evidence of the southward migration of the seismicity comes from sets 12 to 14: We can clearly observe a progressive migration of the hypocenters up to 1.5 km south of the main part of the microseismic cloud. Moreover the "southern" seismicity exhibits a different pattern: Hypocenters are less numerous and distributed over a wide area, so that the seismicity is much sparser than in the northern part of the microseismic cloud, where numerous events define a zone of dense seismicity.

The evolution of the microseismic cloud provides insights regarding the hydraulic diffusivity of the system. First we noticed that the maximum northwestern extension of the activity is reached rather soon (set 5) during the second step of the injection scheme. This also corresponds to the decrease of the pressure response at injection rates of 30 $l.s^{-1}$ and 40 $l.s^{-1}$. These are clear indications that hydraulic diffusion plays a dominant role in the first two steps of the injection to quickly accommodate the amount of injected water. However, as soon as injection at 50 $l.s^{-1}$ is performed, seismicity does not migrate further north-west and the pressure continues to increase. The diffusivity of the medium seems to be too low here to easily spread the additional water over the rock volume. It confirms that the stimulated medium reacts differently to the injection rate of 50 $l.s^{-1}$ The sharp borders of the microseismic cloud, which previously were interpreted as either low or high permeable features, could similarly be associated with either low or high diffusivity material.

Another indication is given by the differences in the depth distribution of the microseismic events: During the first part of the stimulation test the deepest hypocenters that occurred in the northern part of the reservoir extend down to 5.5 km depth, while the southern events mainly occur above 4.8 km depth. The cold, fresh water that is injected into the medium moves downwards in the first part of the stimulation test, because of gravity effects. However, the late and shallower events may be induced by an upward migration of the water which has heated up through its circulation within hot rocks and is consequently less dense.

3.4. High-magnitude Events

In this experiment, which generates microseisms, we consider events of duration magnitude higher or equal to 1 as high-magnitude events. We recorded earthquakes in the

magnitude range –0.9 to 2.5 during the injection period but the most energetic event ($M_d = 2.6$) occurred in the post-fracturation test period. Among the 7,062 events for which we have been able to determine the magnitude, 627 reach magnitude 1 or higher and 26 are equal to or above magnitude 2. Figure 11 depicts their distribution in three dimensions. The radius of each sphere is proportional to the magnitude and the color scale corresponds to the period during which the earthquake occurred. There is one color per day of record, except for the last two days (10th and 11th of July) plotted together under the same color. The evolution of these events follows the same characteristics as the evolution of the whole cloud: The first high magnitude event ($M_d = 1.1$) occurred about half an hour after the beginning of the experiment and the hypocenters tend to move away from the open-hole section of the injection well, even if some of them continue to take place in already stimulated zones. It also appears that the majority of late hypocenters, i.e., hypocenters that occurred after the shut-in, are located in the upper part of the geothermal reservoir, although the other events are equally distributed in the range 4.0 km depth to 5.5 km depth. In particular, they define two distinct areas which are clearly separated from the main microseismic cloud. The first is situated on the north-west of the reservoir and the other is on the south. The feature defined on the north-west shows a large high-magnitude events to low-magnitude events ratio compared to the main seismicity. This could be an indication of a late activated structure controlling the seismicity in this small zone.

Moreover, we studied the largest event that occurred during the stimulation experiment. It took place on 16 July, that is, the day after the end of the post-fracturation test. We estimated its magnitude to be 2.6; unfortunately, the temporary surface network had been removed at that period, so that we computed its location with a limited number of stations. Consequently, we only used the three permanent surface stations of the ReNaSS, the broad-band sensor and three downhole stations. The location is nevertheless reliable, since the rms is equal to 0.01 s. This event is situated in the upper northwestern part of the main microseismic cloud (grey-colored sphere on Fig. 11), but seems to be related to the emergent structure on the north-west: It may have broken a part of the defined structure, which had not sheared yet.

4. Discussion

In order to evaluate the hydro mechanical properties of the reservoir and to characterize its response to the stimulation test from a seismological point of view, we must investigate the correlations between the seismological and hydrological observations.

Analysis of the evolution of the microseismic cloud is a first tool to understand the process of events nucleation under the stimulation conditions. It has been observed at several other HDR sites that the shape and orientation of the microseismic cloud results from the interaction between the pre-existing joints network, the injected fluid and the

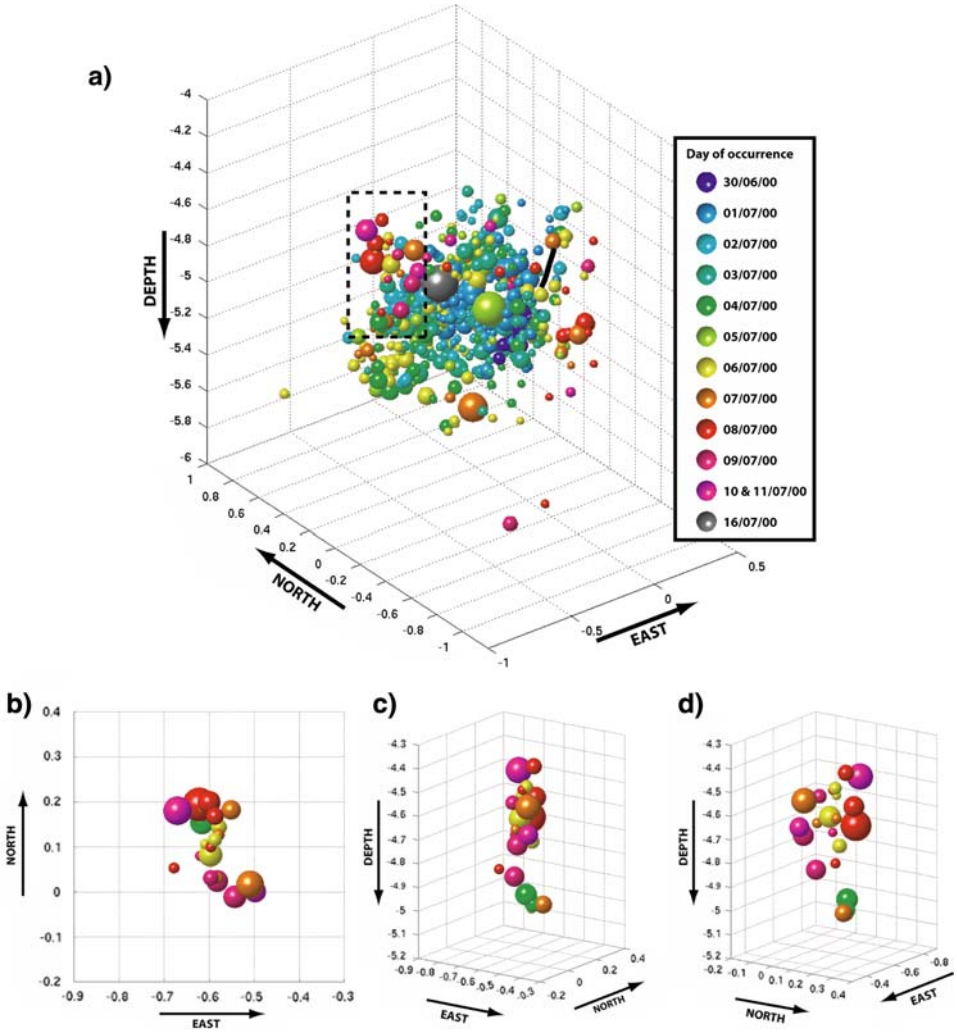

Figure 11

a) Three-dimensional representation of the strongest events which occurred during the 2000 stimulation. Colors correspond to the temporal evolution of the cloud and the radii of the spheres are proportional to the magnitude of the events (magnitude range: 1.0 to 2.6). The black line corresponds to the trajectory of the open-hole section of the well GPK2. b), c) and d) Zoom on the events delineated by the dashed box (magnitude range: 1.0 to 2.2). Color scale is the same as for Figure 9a and the radius of each sphere is still proportional to magnitude. b) Plane view, c) 3-D representation, viewed along the azimuth N55° (direction of minimal extension of the cloud), d) 3-D representation, viewed along the azimuth N145° (direction of maximal extension of the cloud).

stress regime, within which the orientation of the maximum horizontal stress has a prominent role (e.g., PINE and BATCHELOR, 1984; FEHLER *et al.*, 1987; BARIA *et al.*, 1995). Moreover, these observations show that the growth of the seismicity will be largely

controlled by the orientation of the pre-existing seismic structures in respect to the direction of the maximum horizontal stress. Several authors gave estimates of the direction of S_H at Soultz-sous-Forêts from different methods. At regional scale, studies indicate a NW-SE to NNW-SSE orientation of the maximum horizontal stress (e.g., PLENEFISH and BONJER, 1997, from inversion of focal mechanisms). At local scale, that is, at the Soultz site, several methods have been applied to determine the direction of S_H, which seems to slightly differ from large-scale estimates. RUMMEL and BAUMGÄRTNER (1991) obtained a N155°E preferred orientation for S_H to 2000 m depth (with a N176°E second possible solution) from hydraulic stress measurements on pre-existing fractures. KLEE and RUMMEL (1993), using a similar technique, confirmed the N155°E direction for S_H in the upper part of the granite and determined a N170°E trend below. HELM (1996) determined a more NW-SE (N124°E) oriented maximum horizontal stress from the inversion of polarities data. However, other authors suggest a more N-S orientation for S_H, which is presently assumed to be the most reliable estimate. TENZER *et al.* (1991) suggest a N170°E for S_H, from the study of vertical hydraulic-induced fractures and borehole breakouts in the upper 600 m of the granite massif. This result has been extended to about 4300 m by TENZER *et al.* (2000) from additional, deeper measurements. A similar orientation (N175°E) has been given by CORNET and JONES (1994) from the observation of thermal-induced vertical fractures. Recently, BERARD and CORNET (2003) confirmed this direction by the analysis of breakouts and thermal elongation of the boreholes. Moreover, GENTER and TRAINEAU (1996) analyzed macroscopic fractures observed on a continuous granite core section drilled in the observation well EPS1. By comparison between cores and BoreHole TeleViewer imagery, they found two major fractures sets, striking N-S and NNW-SSW, which orientation is suitable for their reactivation within the stress field described above. Figure 9 shows the orientation of the microseismic cloud, which is elongated in a N30°W–N35°W direction. This result is consistent with the orientation of the microseismic clouds, which were induced during previous stimulation experiments at shallower depth in 1993, 1995 and 1996 (JONES *et al.*, 1995, 1996; HELM, 1996; BARIA *et al.*, 1999). Thus, the direction of the cloud's growth seems reasonably to be in agreement with the geometrical pattern of the structures and the stress field. This confirms the role of the regional natural tectonic stress controlling the shearing of fractures. Thus, the hydraulic injections seem not to perturb the overall state of stress in the geothermal reservoir, but just have local effects on fractures planes by increasing the pore pressure.

Another question remains open considering the evolution of the induced seismicity: What does control its final and maximal extension? Two observations lead to this questions: First, we can clearly note on Figure 10 the early migration of the hypocenters to the north-west, which quickly stops at about 1 km NW of the injection well. Until the end of the experiment, the microseismic cloud did not extend more distantly away to the NW, while several isolated events appear to the South. Late microseisms occur up to 1.5 km south of GPK2. The second important observation concerns the depth distribution of the hypocenters (Figure 9): they are distributed between 4 km and 5.5 km depth, but

above 4 km depth and below 5.5 km depth, we cannot observe any events so that the top and bottom boundaries of the cloud look very sharp.

One possible explanation would be the presence of natural features on the north-west of the cloud and at its top and bottom, avoiding the seismicity to migrate. In the case of the stimulation experiment, it implies that these features could be less permeable to the fluid flows and/or pore pressure diffusion or, on the contrary, highly permeable and corresponding to easy flowpaths with no pressure increase then no further microseismic activity. Moreover, the slow decrease of the overpressure in the stimulated volume after the shut-in (Fig. 2) suggests that the geothermal system behaves progressively like a confined system. Therefore late activated flowpaths are necessary to reach permeable and unstimulated zones.

It is interesting to note on Figure 10 that the maximal northwestern extension of the microseismic cloud is reached at set 5. However, events forming the following set (set 6) do not reach the point of maximal extension and they even are 200–250 m before it, while we can see a continuous migration between set 1 and set 5 and later between set 6 and the final set. Moreover, the shape of the microseismic cloud looks totally different: Events of set 5 constitute a thin, elongated ellipse while set 6 looks thicker and more concentrated. Table 1 gives the periods covered by both sets: It appears from Figure 2 that set 6 begins only a few hours after the increase of injection rate from 40 $l.s^{-1}$ to 50 $l.s^{-1}$. It also does correspond to a major change in the evolution of the P-wave velocity structure of the geothermal reservoir, as described in paragraph 3.2. However, no indication of such variations in the evolution of the microseismic cloud and the seismic velocity structure can be seen after the increase from 30 $l.s^{-1}$ (set 3) to 40 $l.s^{-1}$ (set 4). The pressure curve likewise exhibits significant differences depending on the injection rate: while the overpressure reaches a maximum and then slowly decreases when the rate has risen to 30 $l.s^{-1}$ and 40 $l.s^{-1}$, it continues increasing until the shut-in under an injection rate of 50 $l.s^{-1}$. This observation tends to confirm the fact that the geothermal reservoir does not easily accommodate the overpressure and thus behaves like a partially closed system. However this behavior seems to be very dependent on the load. In our case, the injection rate of 50 $l.s^{-1}$ is a sort of threshold, which induces significant change in the hydromechanical response of the stimulated volume.

In order to check the influence of the increase of injection rate on the coefficient of the Gutenberg-Richter curve, we calculated the temporal variations of the *b*-value during the stimulation. We used the maximum likelihood estimate given by Aki (1965) to calculate the *b*-values. We defined a moving window of 500 events overlapping by 250 events. Results are shown on Figure 12 together with the changes of injection rate during the stimulation. Error bounds correspond to the 95 percent confidence limits. There are quite large variations in the evolution of *b* and three peaks corresponding to high *b*-values appear clearly. The first significant increase of *b* seems to be induced by the increase of injection rate from 30 $l.s^{-1}$ to 40 $l.s^{-1}$. Moreover, the response of the reservoir to this perturbation is almost instantaneous. Thus, such a rapid change of the injection rate is likely to produce a large proportion of small events, corresponding to a high *b*-value.

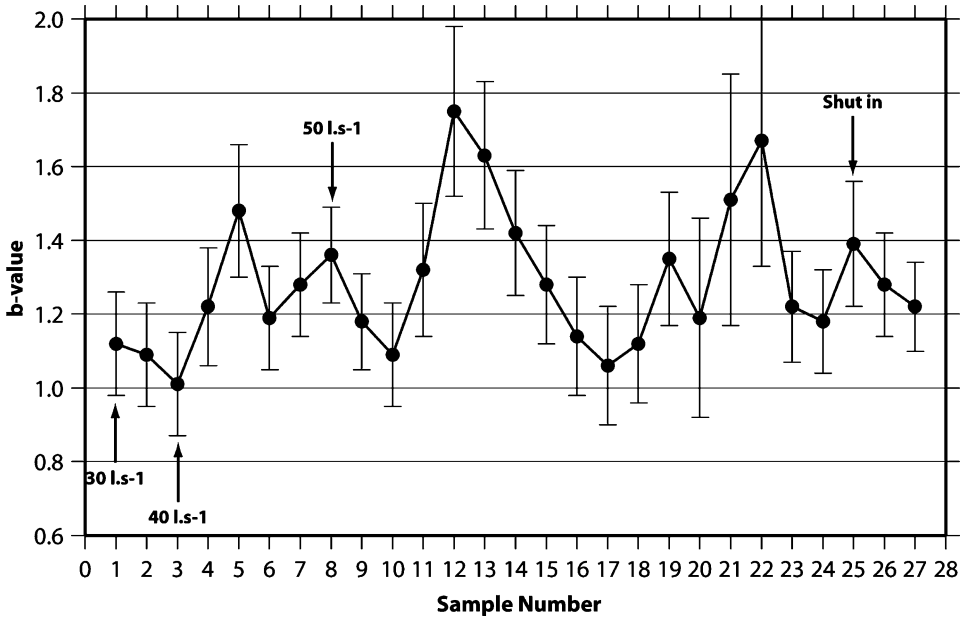

Figure 12
Evolution of the *b*-value during the stimulation test. *b*-values are plotted with their corresponding error bounds indicating the 95 percent confidence level. Changes of injection rate are also indicated. Each sample contains 500 events, overlapping by 250 events.

HENDERSON *et al.* (1999) also reported this process from the analysis of injection-induced seismicity in The Geysers geothermal area (California). We could expect the same behavior when the rate has increased to 50 $l.s^{-1}$, but on the contrary, we note a decrease of the *b*-value, followed by another rise. The immediate response of the rock massif acts nevertheless in the opposite way as the first change of injection rate (30 $l.s^{-1}$ to 40 $l.s^{-1}$). This can be related to the fact that we observe clear variations in the evolution of the seismic velocity structure and the distribution of hypocenters when the rate increases to 50 $l.s^{-1}$ although we see no such differences between 30 $l.s^{-1}$ and 40 $l.s^{-1}$. Thus, both rates induce changes in the behavior of the stimulated volume but not in the same manner. Furthermore, the presence of the significant peak following the decrease associated with the rate of 50 $l.s^{-1}$ suggests that the instantaneous response, i.e., the drop of the *b*-value, corresponds only to a transient process, during which the fluid reaches already extensively stimulated zone. Numerous fractures, which could have generated small events, have already slipped and the increase of pore fluid pressure is not large enough to induce another shearing on these fractures plane. Then the expected effect due to the increase of injection rate is delayed until fluids reach less stimulated zones and/or until the overpressure is sufficiently high to induce another shearing. The same process could explain the decrease of *b*-value at the beginning of the experiment. The well GPK2

underwent several hydraulic tests, such as a slug test, a production test and a low-flow injection test before being massively stimulated. Then, despite a lower level of generated overpressure due to low injection rate, some small fractures in the near-well zone may have already sheared during these previous hydraulic tests and the early beginning of the stimulation: They are not reactivated afterwards under a load of 30 $l.s^{-1}$. This "oscillatory" behavior of the *b*-values may indicate that small fractures are shearing first, forming a stimulated zone where flowpaths have been created, and where fluid can easily propagate up to an area where the hydraulic diffusivity is lower: Here pressure is likely to increase and induce shear on a new reactivated fault plane. On another hand, the decrease of the *b*-value following the shut-in may involve other mechanisms. Despite their drop, *b*-values remain at a higher level (between 1.2 and 1.4) than at the beginning of the stimulation test. Nevertheless we observe a larger proportion of big events after the shut-in. For example, we note eights events of magnitude higher or equal to 2 among the 700 earthquakes which occurred after the end of the injection, whereas 18 events among 6,362 are above magnitude 2 during the injection phase. Then, with respect to the total number of events in each period, we observed four times more big earthquakes after the shut-in than during the injection. Moreover the highest magnitude event (16/07/00, $M_d = 2.6$) took place the day after the end of the post-stimulation test. Thus it seems that the overall pressure relaxation process in the stimulated volume generates on one hand a lesser number of microseisms because of the global fall of the overpressure in the reservoir, but on the other hand, the quickness of the instantaneous pressure drop (about 5 MPa in a few hours on Fig. 2) may have induced some strong local stress heterogeneities on appropriate fracture planes to generate higher magnitude events. However the fact that a lesser proportion of higher magnitude events occur during injection, that is during periods of strong overpressure has to be explained. The geometry of the fracture network could be a cause: Genter and Traineau (1996) have shown that large fault zones exist, within which numerous small-scale fractures appear to be "en échelon". It is likely that overpressures induce shearing on these small fracture planes, which may slip one after the other. The whole fault zone does indeed not slip in only one, big displacement, preventing the nucleation of larger magnitude events. On the contrary, the relaxation process at the shut-in may act on the whole fault zones differently and induce larger displacements.

Finally it is interesting to note from Figure 11 that at least a part of these big earthquakes forms some clusters within the microseismic cloud, such as the structure described in paragraph 3.4; it could indicate that the fluid injection reactivated some faults whose dimensions allow the nucleation of events exceeding magnitude 2. However, the frequency-magnitude distribution (Fig. 5) shows that the distribution of earthquakes of magnitude higher than 1.8 falls below the slope representing the Gutenberg-Richter law. This means that there is a strong lack of such events in comparison with the distribution of small microseisms. It suggests that either there are very few fractures within the granite massif which could produce events of magnitude higher than 2 (even no fracture for $M \geq 3$ events, as the $M_d = 2.6$ earthquake was the

strongest ever recorded at the site of Soultz-sous-Forêts during all stimulation tests) or, if they really exist, they could be not activated yet because they still do not reach their critical state of stress. Another explanation could be that these fractures could have slipped in small parts and not on a whole, producing a smaller magnitude than we can expect.

5. Conclusion

The seismicity induced by fluid injection during the 2000 stimulation experiment at the geothermal site of Soultz-sous-Forêts forms a dense microseismic cloud, which shows a flat ellipsoid shape. Its extension fits with the direction of the maximal horizontal stress of the regional tectonic stress field, which controls the overall slipping on the fractures planes, but event nucleation is probably induced by local stress heterogeneities due to the increase of pore fluid pressure in the vicinity of the faults. The evolution of the microseismic cloud is highly dependent on the injection rate, as each variation (increase or decrease of the rate) leads to changes of the behavior of the stimulated rock volume. It affects the seismic velocity structure, the number and magnitude of generated events, their distribution within the stimulated volume and involves different hydro mechanical processes responsible for the final shape of the microseismic cloud. Furthermore, for a future industrial exploitation and from a seismic risk point of view, the study shows that the hydraulic stimulation tends to induce a large proportion of small earthquakes ($M \leq 1$), even if we identify some structures which can produce events of magnitude higher than 2. Nevertheless the frequency-magnitude distribution of the whole induced seismicity shows that these "big" events are lacking with respect to the small events and that magnitude 3 seems to be the maximal magnitude which could be reached under the same conditions of injection, except if the stimulation tests have to date induced shear on only subsidiary parts of major fault zones.

References

Aki, K. (1965), *Maximum likelihood estimate of b in the formula log N = a-bM and its confidence limits*, Bull. Earthq. Res. Inst. *43*, 237–239 (University of Tokyo).

Baria, R., Garnish, J., Baumgärtner, J., Gérard, A., and Jung, R. (1995), *Recent development in the European HDR research programme at Soultz-sous-Forêts (France)*. In: *Proc. World Geothermal Congress*, Florence, Italy, International Geothermal Association, pp. 2631–2637.

Baria, R., Gérard, A., Baumgärtner, J., and Garnish, J. (1996), *Progress at the European HDR site at Soultz, France*. In *3rd International HDR Forum, Proceedings*, Santa Fe, USA, 1996 (ed. Duchane, D. V.), pp. 73–74.

Baria, R., Baumgärtner, J., Gérard, A., Jung, R., and Garnish, J. (1999), *European HDR research programme at Soultz-sous-Forêts (France) 1987–1996*, Geothermics *28*, 655–669.

Baria, R., Baumgärtner, J., Gérard, A., and Garnish, J. (2000), *The European HDR programme: Main targets and results of the deepening of the well GPK2 to 5000 m*. In: *Proc. World Geothermal Congress*, Kyushu-Tohoku, Japan, International Geothermal Association, pp. 3643–3652.

BARIA, R., BAUMGÄRTNER, J., GÉRARD, A., WEIDLER, R., and HOPKIRK, R. (2001), *European Hot Dry Rock geothermal research programme 1998–2001*, Final Report (publishable) to European Commission, April 1998-June 2001, Contract n. JOR3-CT98–0313, 89 pp.

BAUMGÄRTNER, J., GÉRARD, A., and BARIA, R. (2000), *Soultz-sous-Forêts: Main technical aspects of deepening the well GPK2*. In *Proc. World Geothermal Congress*, Kyushu-Tohoku, Japan, International Geothermal Association, pp. 3653–3663.

BEAUCE, A., FABRIOL, H., LE MASNE, D., CAVOIT, C., MECHLER, C., and CHEN, X. (1991), *Seismic studies on the HDR site of Soultz-sous-Forêts (Alsace, France)*, Geotherm. Sci. Technol. *3*, 239–266..

BENDERITTER, Y. and ELSASS, P. (1995), *Structural control of deep fluid circulation at the Soultz HDR site, France: A review*, Geotherm. Sci. Technol. *4*, 227–237.

BÉRARD, T. and CORNET, F. H. (2003), *Evidence of thermally induced borehole elongation: A case study at Soultz, France*, Int. J. Rock Mech. Min. Sci. *40*, 1121–1140.

CHRISTENSEN, N.I., and WANG, H.F. (1985), *The influence of pore pressure and confining pressure on dynamic elastic properties of Berea sandstones*, Geophysics *50*, 2, 207–213.

CORNET, F.H. and JONES, R. (1994), *Field evidence on the orientation of forced water flow with respect to the principal stress directions*. In *Proc. 1st North Amer. Rock Mech. Symp.* (eds. Nelson and Laubach) (Balkema, Rotterdam 1994), pp. 61–69.

CORNET, F.H. and YIN, J. (1995), *Analysis of induced seismicity for stress field determination and pore pressure mapping*, Pure Appl. Geophys. *145*, 677–700.

CORNET, F.H., HELM, J., POITRENAUD, H., and ETCHECOPAR, A. (1997), *Seismic and aseismic slip induced by large-scale fluid injections*, Pure Appl. Geophys. *150*, 563–593.

DELÉPINE, N. (2003), *Etude d'anisotropie à Soultz-sous-Forêts*, Mémoire de D.E.A., Ecole et Observatoire des Sciences de la Terre, Université Louis Pasteur, Strasbourg, France, 36 pp.

DYER, B.C. (2001), *Soultz GPK2 stimulation June/July 2000. Seismic monitoring report*, Semore Seismic Report.

EBERHART-PHILLIPS, D., *Local tomography: Earthquake source regions*. In *Seismic Tomography: Theory and Practice* (eds. Iyer H.M. and Hirahara K.) (Chapman and Hall, New-York 1993), pp. 613–643.

EVANS, J.R., EBERHART-PHILLIPS, D., and THURBER, C.H. (1994), *User's manual for SIMULPS12 for imaging V_p and V_p/V_s, a derivative of the Thurber tomographic inversion SIMUL3 for local earthquakes and explosions*, U.S. Geol. Surv. Open-File Rep. *94–431*, 142 pp.

FEHLER, M. C., HOUSE, L. S., and KAIEDA, H. (1987), *Determining planes along which earthquakes occur: Method and application to earthquakes accompanying hydraulic fracturing*, J. Geophys. Res. 92, 9407–9414.

FEHLER, M.C., PHILLIPS, W.S., HOUSE, L.S., JONES, R.H., ASTER, R.C., and ROWE, C.A. (2000), *Improved relative locations of clustered earthquakes using constrained multiple event location*, Bull. Seismol. Soc. Am. *90*, 775–780.

GARNISH, J., BARIA, R., BAUMGÄRTNER, J., and GÉRARD, A. (1994), *The European Hot Dry Rock programme 1994–95*, Geothermal Resources Council Transactions *18*, 431–438.

GAUCHER, E., CORNET, F.H., and BERNARD, P. (1998), *Induced seismicity analysis for structure identification and stress field determination*, Proc. SPE-ISPM *Rock Mechanics in Petroleum Engineering Conference 1*, 545–554.

GENTER, A. and TRAINEAU, H. (1996), *Analysis of macroscopic fractures in granite in the HDR geothermal well EPS-1, Soultz-sous-Forêts*, France, J. Volc. Geotherm. Res. 72, 121–141.

GENTER, A., CASTAING, C., DEZAYES, C., TENZER, H., TRAINEAU, H., and VILLEMIN, T. (1997), *Comparative analysis of direct (core) and indirect (borehole imaging tools) collection of fracture data in the Hot Dry Rock Soultz reservoir (France)*, J. Geophys. Res. *102* (B7), 15419–15431.

GÉRARD, A., BAUMGÄRTNER, J., and BARIA, R. (1997), *An attempt towards a conceptual model derived from 1993–1996 hydraulic operations at Soultz*. In *Proc. NEDO Internat. Symp.* Sendai, Japan. *2*, pp. 329–341.

GUTENBERG, R. and RICHTER, C.F. (1944), *Frequency of earthquakes in California*, Bull. Seismol. Soc. Am. *34*, 185–188.

HEALY, J.H., RUBEY, W.W., GRIGGS, D.T., and RALEIGH, C.B. (1968), *The Denver earthquake*, Science *161*, 1301–1310.

HELM, J.A. (1996), *The natural seismic hazard and induced seismicity of the European Hot Dry Rock geothermal energy project at Soultz-sous-Forêts (Bas-Rhin, France)*, Thèse de Doctorat, Ecole et Observatoire des Sciences de la Terre, Université Louis Pasteur, Strasbourg, France, 197 pp.

HENDERSON, J.R., BARTON, D.J., and FOULGER, G.R. (1999), *Fractal clustering of induced seismicity in The Geysers geothermal area, California*, Geophys. J. Int. *139*, 317–324.

JONES, R.H. (1999), Modelling of Soultz microseismic performance with an additional sensor, CSMA Internal Report IR03/83.

JONES, R.H., BEAUCE, A., JUPE, A., FABRIOL, H., and DYER, B.C. (1995), *Imaging induced microseismicity during the 1993 injection tests at Soultz-sous-Forêts*. In: *Proc. World Geothermal Congress*, Florence, Italy, International Geothermal Association, pp. 2665–2669.

JONES, R.H., BEAUCE, A., BITRI, A., and WILSON, S. (1996), *The analysis and interpretation of microseismicity induced during the 1995 stimulation and circulation experiments at the European HDR project at Soults-sous-Forêts, France*. In *Proc. 3rd Internat. HDR Forum*, Santa Fe, USA, 1996 (ed. Duchane, D.V.), pp. 81–82.

JONES, R.H. and STEWART, R.C. (1997), *A method for determining significant structures in a cloud of earthquakes*, J. Geophys. Res. *102 (B4)*, 8245–8254.

JUNG, R. (1991), *Hydraulic fracturing and hydraulic testing in the granitic section of borehole GPK1, Soultz-sous-Forêts*, Geotherm. Sci. Technol. *3*, 149–198.

JUNG, R., WILLIS-RICHARD, J., NICHOLLS, J., BERTOZZI, A., and HEINEMANN, B. (1995), *Evaluation of hydraulic tests at Soultz-sous-Forêts, European HDR site*. In *Proc. World Geothermal Congress*, Florence, Italy, International Geothermal Association, pp. 2671–2676.

KAPPELMEYER, O., GÉRARD, A., SCHLOEMER, W., FERRANDES, R., RUMMEL, F., and BENDERITTER, Y. (1991), *European HDR project at Soultz-sous-Forêts, General presentation*, Geotherm. Sci. Technol. *2*, 263–289.

KING, M.S. (1966), *Wave velocities in rocks as a function of changes in overburden pressure and pore fluid saturants*, Geophysics *31*, 1, 50–73.

KLEE, G. and RUMMEL, F. (1993), *Hydrofrac stress data for the European HDR research project test site Soultz-sous-Forêts*, Int. J. Rock Mech. Min. Sci. and Geomech. Abstr. *30*, 973–976.

MORIYA, H., NAKAZATO, K., NIITSUMA, H., and BARIA, R. (2002), *Detailed fracture system of the Soultz-sous-Forêts HDR field evaluated using microseismic multiplet analysis*, Pure. Appl. Geophys. *159*, 517–541.

MURRU, M., MONTUORI, C., WYSS, M., and PRIVITERA E. (1999), *The location of magma chambers at Mt. Etna, Italy, mapped by b-values*, Geophys. Res. Lett. *26*, 2553–2556.

NUR, A., *Seismic rock properties for reservoir descriptions and monitoring*. In *Seismic tomography - With applications in global seismology and exploration geophysics* (ed. Nolet G.) (D. Reidel Publishing Company, Dordrecht 1987), pp. 203–237.

NUR, A. and SIMMONS, G. (1969a), *The effect of saturation on velocity in low porosity rocks*, Earth Planet. Sci. Lett. *7.*, 183–193.

PEARSON, C. (1981), *The relationship between microseismicity and high pore pressures during hydraulic stimulation experiments in low permeability granitic rocks*, J. Geophys. Res. *86*, 7855–7864.

PHILLIPS, W.S. (2000), *Precise microearthquake locations and fluid flow in the geothermal reservoir at Soultz-sous-Forêts, France*, Bull. Seismol. Soc. Am. *90*, 212–228.

PINE, R. J. and BATCHELOR, A. S. (1984), *Downward migration of shearing in jointed rock during hydraulic injections*, Int. J. Rock Mech. Min. Sci. and Geomech. Abstr. *21*, 249–263.

PLENEFISH, T. and BONJER, K.-P. (1997), *The stress field in the Rhine Graben area inferred from earthquake focal mechanisms and estimation of frictional parameters*, Tectonophysics *275*, 71–97.

PRIBNOW, D., FESCHE, W., and HÄGEDORN, F. (1999), *Heat production and temperature to 5 km depth at the HDR site in Soultz-sous-Forêts*, GGA Report 0 119 144, Project BMBF 032 66 90 A, 19 pp.

PUJOL, J. (1992), *Joint hypocentral location in media with lateral velocity variations and interpretation of the station corrections*, Phys. Earth Planet. Inter. *75*, 7–24.

ROWE, C.A., ASTER, R.C., PHILLIPS, W.S., JONES, R.H., BORCHERS, B., and FEHLER, M.C. (2002), *Using automated, high-precision repicking to improve delineation of microseismic structures at the Soultz geothermal reservoir*, Pure Appl. Geophys. *159*, 563–596.

RUMMEL, F. and BAUMGÄRTNER, J. (1991), *Hydraulic fracturing stress measurements in the GPK1 borehole, Soultz-sous-Forêts*, Geotherm. Sci. Technol. *3*, 119–148.

SCHELLSCHMIDT, R. and SCHULZ, R. (1991), *Hydrothermic studies in the Hot Dry Rock project at Soultz-sous-Forêts*, Geotherm. Sci. Technol. *3*, 217–238.

TENZER, H., MASTIN, L., and HEINEMANN, B. (1991), *Determination of planar discontinuities and borehole geometry in the crystalline rock of borehole GPK1 at Soultz-sous-Forêts*, Geotherm. Sci. Technol. *3*, 31–67.

TENZER, H., SCHANZ, U., and HOMEIER G. (2000), *Development and characterization of a HDR heat exchanger at the HDR test site at Soultz-sous-Forêts: Flow logs, joint systems and hydraulic active fractures*. In *Proc. World Geothermal Congress*, Kyushu-Tohoku, Japan, International Geothermal Association, 3921–3926.

THURBER, C.H. (1983), *Earthquake locations and three-dimensional crustal structure in the Coyote Lake area, Central California*, J. Geophys. Res. *88 (B10)*, 8226–8236.

TODD, T. and SIMMONS, G. (1972), *Effect of pore pressure on the velocity of compressional waves in low-porosity rocks*, J. Geophys. Res. *77*, 20, 3731–3743.

TRAINEAU, H., GENTER, A., CAUTRU, J.P., FABRIOL, H., and CHEVREMONT, P. (1991), *Petrography of the granite massif from drill cutting analysis and well log interpretation in the geothermal HDR borehole GPK1 (Soultz, Alsace, France)*, Geotherm. Sci. Technol. *3*, 1–29.

WEIDLER, R., GÉRARD, A., BARIA, R., BAUMGÄRTNER, J., and JUNG, R. (2002), *Hydraulic and micro-seismic results of a massive stimulation test at 5 km depth at the European Hot-Dry-Rock test site Soultz, France*. In *Proc. 27th Workshop on Geothermal Reservoir Engineering*, Stanford University, Stanford, USA, January 2002.

WYLLIE, M.R., GREGORY, A.R., and GARDNER, L.W. (1956), *Elastic wave velocities in heterogeneous and porous media*, Geophysics *21*, 41–70.

WYLLIE, M.R., GREGORY, A.R., and GARDNER, L.W. (1958), *An experimental investigation of factors affecting elastic wave velocities in porous media*, Geophysics *23*, 459–493.

WYSS, M., KLEIN, F., NAGAMINE, K., and WIEMER, S. (2001), *Anomalously high b-values in the South Flank of Kilauea volcano, Hawaii: Evidence for the distribution of magma below Kilauea's East rift zone*, J. Volc. Geotherm. Res. *106*, 23–37.

(Received June 28, 2004, revised May 5, 2007, accepted November 12, 2007)
Published Online First: May 10, 2008